AIP | Physics of Fluids

Far-field momentum flux of high-frequency axisymmetric synthetic jets

X. Xia and K. Mohseni

Citation: Physics of Fluids **27**, 115101 (2015); doi: 10.1063/1.4935011
View online: http://dx.doi.org/10.1063/1.4935011
View Table of Contents: http://scitation.aip.org/content/aip/journal/pof2/27/11?ver=pdfcov
Published by the AIP Publishing

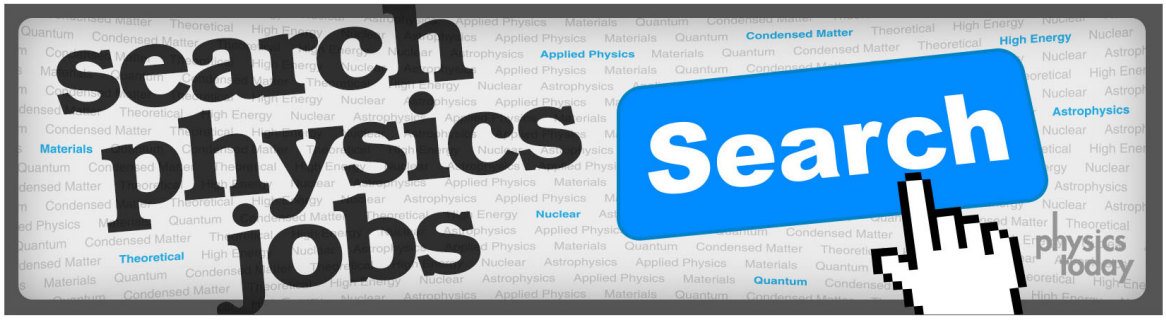

PHYSICS OF FLUIDS **27**, 115101 (2015)

Far-field momentum flux of high-frequency axisymmetric synthetic jets

X. Xia[1] and K. Mohseni[1,2,3,a)]
[1]*Department of Mechanical and Aerospace Engineering, University of Florida, Gainesville, Florida 32611-6250, USA*
[2]*Department of Electrical and Computer Engineering, University of Florida, Gainesville, Florida 32611-6250, USA*
[3]*Institution for Networked Autonomous Systems, University of Florida, Gainesville, Florida 32611-6250, USA*

(Received 8 May 2015; accepted 20 October 2015; published online 4 November 2015)

This study focuses on predicting the far-field momentum flux for axisymmetric synthetic jets, which is an important parameter that characterizes the performance of such jets in flow-control applications. Previous researchers have found that a negative pressure gradient near the jet orifice is responsible for the observed decrease in the momentum flux in the streamwise direction. As a result, prediction of the far field momentum flux of synthetic jets has encountered serious challenges. In this paper, the far-field momentum flux is modeled by calculating the hydrodynamic impulse of the vortical structure formed during one actuation cycle, under the assumption that the jet is fully developed and periodic. In this manner, the complex near-field effect of a synthetic jet is explicitly captured by the interactions between the vortices and the actuator. Furthermore, the impulse of these vortical structures is predicted using only the actuation parameters of the synthetic jet, namely, the stroke length, L, the orifice diameter, d, and the actuation frequency, f. For a synthetic jet with a stroke ratio, L/d, larger than the formation number, L^*/d, this model predicts that the normalized far-field momentum flux, K/K_s, decreases when L/d increases. This can be explained by an increasing circulation fraction of the trailing jet, which contains less impulse per unit circulation compared with the leading vortex. This model is validated using hot-wire anemometry measurement of a series of synthetic jets. Moreover, by comparing with experimental data that have large L/d, this model suggests that the contribution of trailing jet to the overall far-field momentum flux is not negligible. © *2015 AIP Publishing LLC.* [http://dx.doi.org/10.1063/1.4935011]

I. INTRODUCTION

Synthetic jets are pulsatile jets with a zero-net-mass-flux (ZNMF) property at the jet exit plane, meaning that no propellant is required for jetting to take place. Moreover, due to the compactness and low energy consumption of the actuators, synthetic jets have been applied to a variety of applications,[1,2] such as boundary layer separation control,[3–6] flow control over airfoils,[7–11] and underwater vehicle propulsion and maneuvering.[12,13] These applications imply a preexisting background flow of some kind; however, the focus of the current work is on synthetic jets in a quiescent environment, although we note that several researchers have investigated the interaction between synthetic jets and background flow configurations.[8,14–18] In the near field of a synthetic jet (depicted in Fig. 1), axisymmetric vortices are generated, advected away from the exit, and experience continued mutual interaction until a fully developed, turbulence-dominated far field is achieved.[19] This formation process is responsible for the enhanced entrainment and mixing of synthetic jets as compared to continuous jets.[20,21] Furthermore, due to the pulsation of the jets, the near-field

a)Author to whom correspondence should be addressed. Electronic mail: mohseni@ufl.edu

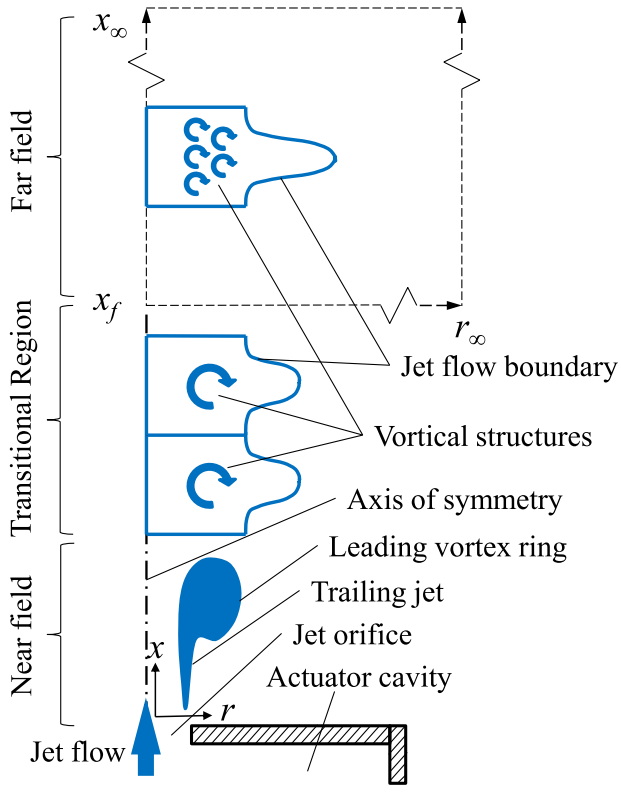

FIG. 1. Schematic showing the flow field of a synthetic jet. The near-field flow is characterized by a strong periodic flow. In the transitional region, the vortex rings interact with each other and the background flow and entrain surrounding fluid. In the far field, the major vortex rings break down into smaller vortices and the flow becomes a turbulent jet. The transition between these different regions is determined by a combined effect of the stroke ratio and the Reynolds number. The Reynolds numbers of the synthetic jets in this study range from 548 to 8781.

flow is highly unsteady and so characterization of the effectiveness of synthetic jets through direct modeling of the near field is quite difficult. Hence, in this study, we pursue the development of a connection between the synthetic jet actuator parameters and the far-field flow.

Recently, Xia and Mohseni[22] developed a model to predict the far-field features of a synthetic jet. Their data showed that the momentum flux, together with an effective eddy viscosity, dictate the spreading and decay behaviors of any jet in the far field. Moreover, the momentum flux is strongly linked to the propulsion of vortex thrusters[13,23,24] and is also important in dictating the performance of a synthetic jet actuator in flow control applications.[3,4,8,9,25] In these studies, the jet effectiveness is typically characterized by the momentum coefficient,[7] C_μ, which is defined as the ratio between the time-averaged jet momentum flux and the characteristic freestream momentum flux. In other studies, the blowing ratio defined as the jet-to-freestream velocity ratio has also been reported to gauge the interactions between synthetic jets and crossflow boundary layers.[16,26–31] The estimation of the blowing ratio involves calculating the jet velocity, which is implicitly related to the momentum flux of the jet. Therefore, the utility of developing an accurate model for the far-field momentum flux of a synthetic jet is apparent.

Traditionally, a slug flow model[32] has been used to obtain a simple estimation of the jet momentum flux. However, investigations employing particle image velocimetry (PIV) techniques to calculate the time-averaged momentum flux at the jet exit[33] and in the near field[34] have shown that the slug model does not always offer a sufficient level of accuracy in predicting the momentum flux of round synthetic jets. Smith and Glezer[19] studied the variation of the far-field momentum flux, as determined from the convective flux of momentum, and found that it decreases with increasing axial distance from the actuator but eventually reaches an asymptotic value, indicating the conservation of momentum in the far field of synthetic jets. They attributed the apparent decrease in

the momentum flux to the presence of an adverse pressure gradient in the near field; Smith and Swift[20] and Shuster and Smith[34] made similar observations and conclusions. However, this pressure gradient in the near field, caused by the alternating processes of suction and ejection, is difficult to model. This is because the flow field near a synthetic-jet orifice is highly pulsatile and vortical. The unsteady nature of the flow, together with the complex geometry of the jet exit, presents a significant challenge for finding an analytical solution to the problem. In light of these considerations, a model for the far-field momentum flux that is based on the pressure gradient mechanism will suffer from similar difficulties. Frequency is also related to the accuracy of momentum-flux estimation using the slug model. Krieg and Mohseni[13] studied the thrust generated by low-frequency ($f \sim 10^1$ Hz) synthetic jets and observed (see Fig. 8 of Krieg and Mohseni[13]) good agreement with the slug model at very low frequencies ($f < 5$ Hz). However, as the frequency is increased, the model begins to overestimate the normalized thrust, which is closely related to the normalized momentum flux. This indicates that a stronger pulsation of a synthetic jet would cause the momentum flux to decrease. Again, the seemingly different physics between low and high frequencies are related to the interactions between vortices as well as the suction effect. Specifically, if other conditions remain the same, a higher frequency would cause the neighboring vortices to be closer to each other and increase the influence of the suction flow. However, as the frequency is increased above 20 Hz, the normalized thrust appears to saturate and be independent of the frequency. This saturation event further indicates that a model independent of frequency could exist for synthetic jets with high frequency.

To avoid dealing directly with the effects of the time-dependent near field, we use an approach that considers the hydrodynamic impulse of the fully developed vortical structure that exits the near field, or equivalently, that eventually enters the far field. First, the change in the far-field momentum is related to the associated hydrodynamic impulse, and then this impulse is connected to that of the vortical structure entering the far field. Finally, the impulse of the vortical structure, and hence the far-field momentum flux, can be related to the jet actuation parameters. This final step, that is, the relationship between the jet actuation parameters and the evolution of the ejected vorticity (usually taking the form of a vortex ring), has been the focus of many other studies[34–43] and so strengthens the reliability of the proposed model to predict the far-field momentum flux.

This article is organized as follows: Section II describes the modeling of the far-field momentum flux for a synthetic jet using the jet-formation parameters. Section III introduces the experimental setup and methods. Section IV briefly discusses the turbulent nature of the jets. Section V presents the results and discussion associated with the model validation, as well as physical insights. Finally, concluding remarks are given in Section VI.

II. THEORETICAL MODELING

A. Far-field momentum flux for synthetic jets

Xia and Mohseni[22] proposed a unified far field model for both synthetic and continuous jets. Two governing parameters, namely, the far-field momentum flux and the effective eddy viscosity, were identified as determining the characteristics of the far field for any turbulent jet. Here, we focus on modeling the (kinematic) time-averaged momentum flux of the jet (per unit density, in the axial direction), K, which is defined as

$$K = \frac{2\pi}{T}\int_0^T \int_0^\infty u^2 r \mathrm{d}r\mathrm{d}t, \tag{1}$$

where T is the period of the actuator and u is the time-varying axial velocity that depends on both r and t. Note that this equation is specific to axisymmetric jets. To predict the far-field behaviors of synthetic jets without any flow field measurement, K must be modeled using the jet-formation parameters, i.e., the stroke length, L, diameter of the jet exit, d, and the driving frequency, f. We now begin to develop the new model for the far-field momentum flux of a synthetic jet.

We start by relating the change in the far-field momentum to the corresponding hydrodynamic impulse. The schematic in Fig. 2 illustrates the evolution of vortical structures in the flow field

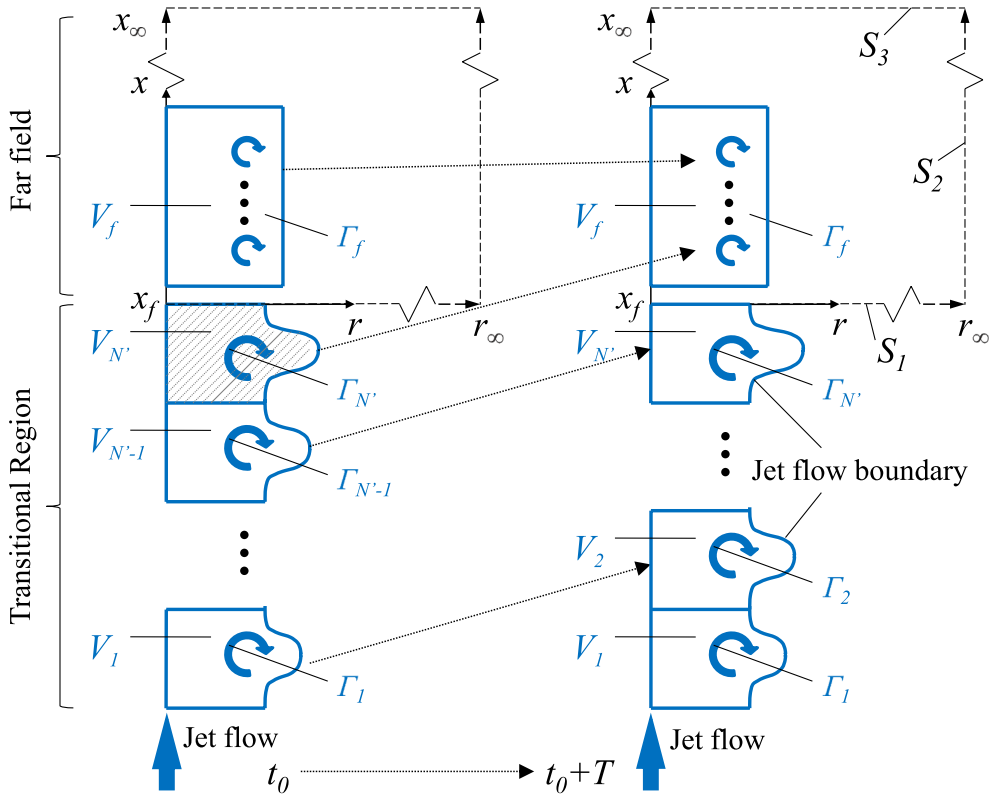

FIG. 2. Schematic showing the periodic evolution of the vortical structures from $t = t_0$ to $t_0 + T$. S_1 is the boundary corresponding to the beginning of the far field, and S_2 and S_3 are control surfaces located at infinity. The vortical structures in the far field are grouped into a finite volume V_f, while outside the far field the individual vortical structures, V_i, are assumed to be isolated control masses. From $t_0 \to t_0 + T$, $V_i \to V_{i+1}$, where $V_{N'+1}$ becomes part of V_f and V_1 is replaced by the newly generated vortical structure from the synthetic jet.

of an axisymmetric synthetic jet, where the two different instances are separated by one period, $T = 1/f$. The far field is regarded as being a control volume which is enclosed by surfaces S_1, S_2, and S_3. The linear momentum, $\vec{M}_f$, within the control volume can be expressed in terms of the corresponding hydrodynamic impulse, $\vec{I}_f$ (defined in Eq. (A1a)), plus a boundary flux term by using a vector/integral identity (Saffman,[44] page 51) as

$$\vec{M}_f(t) = \vec{I}_f(t) + \frac{1}{2}\int_{S_1+S_2+S_3} [\vec{u}(t)(\vec{n}\cdot\vec{x}) - \vec{n}(\vec{u}(t)\cdot\vec{x})]\,\mathrm{d}S, \tag{2}$$

where $\vec{u}$ is the velocity field, $\vec{n}$ is the normal vector of the integrating surface, and $\vec{x}$ is the position vector. The far-field momentum is then obtained by placing the control surface S_1 at $x = x_f$, which is defined to be the axial location of the far-field region. The control surfaces S_2 and S_3 are assumed to be at infinity where the jet vanishes and so the velocity is zero, meaning that the associated surface integrals in Eq. (2) are also zero. Now, since the flow is turbulent and assuming periodicity at S_1, the velocities for different periods are related to each other as

$$\vec{u}(t_0 + mT) - \vec{u}'(t_0 + mT) = \vec{u}(t_0) - \vec{u}'(t_0) = \vec{\bar{u}}(t_0), \tag{3}$$

where $\vec{u}'$ and $\vec{\bar{u}}$ represent the turbulent fluctuation and the mean value, respectively, with the latter satisfying $\vec{\bar{u}}(t_0) = \vec{\bar{u}}(t_0 + mT)$. Also, m is an integer ranging from 0 to N, with N being the total number of periods sampled for the measurement of the momentum flux (N is usually the product of the jet frequency and the sampling time). Note that in reality, the assumed periodicity condition places a further requirement on the definition of the far field location x_f. Evaluating Eq. (2) at $t = t_0$ and $t_0 + NT$ and then subtracting yield

$$\vec{M}_f(t_0+NT)-\vec{M}_f(t_0)=\vec{I}_f(t_0+NT)-\vec{I}_f(t_0)$$
$$+\frac{1}{2}\int_{S_1}\{[\vec{u}'(t_0+NT)-\vec{u}'(t_0)](\vec{n}\cdot\vec{x})-\vec{n}[(\vec{u}'(t_0+NT)-\vec{u}'(t_0))\cdot\vec{x}]\}\,\mathrm{d}S. \tag{4}$$

This is the change in the far-field total momentum within N periods, which is equivalent to the time-integral of the far-field momentum flux across S_1 during the same period. To simplify this equation, $\vec{x}$ can be expressed as $x\vec{e}_x+r\vec{e}_r$, where $\vec{e}_x$ and $\vec{e}_r$ are the unit vectors in the axial and radial directions, respectively. Together with the observation that on the surface S_1 the unit surface normal vector satisfies $\vec{n}=-\vec{e}_x$, the integral in Eq. (4) can be written as

$$\frac{1}{2}\int_{S_1}\{[u_r'(t_0+NT)-u_r'(t_0)](-x\vec{e}_r)+[u_r'(t_0+NT)-u_r'(t_0)](r\vec{e}_x)\}\,\mathrm{d}S, \tag{5}$$

where $\vec{u}'=u_x'\vec{e}_x+u_r'\vec{e}_r$, with u_x' and u_r' being the axial and radial components of the turbulent fluctuation, respectively. Furthermore, since the jet is axisymmetric, the radial component of Eq. (5) is zero, as well as the radial components of the momentum and hydrodynamic impulse. By writing $\vec{M}_f=M_f\vec{e}_x$ and $\vec{I}_f=I_f\vec{e}_x$, the time-averaged axial momentum flux into the far field is then calculated to be

$$K(x_f)=\frac{M_f(t_0+NT)-M_f(t_0)}{NT}$$
$$=\frac{I_f(t_0+NT)-I_f(t_0)}{NT}+\frac{1}{2NT}\int_{S_1}[u_r'(t_0+NT)-u_r'(t_0)]r\mathrm{d}S. \tag{6}$$

Inspection of Eq. (4) shows that the boundary flux contribution to the *change* in the far-field momentum is entirely associated with turbulent fluctuations of the velocity field at the surface S_1; Eq. (6) provides the further result that the contribution is from fluctuations of the radial velocity. Again, this result is contingent on the periodicity condition being satisfied at x_f in the far field. Now, since Eq. (6) represents the time-averaged axial momentum flux, then by definition of a turbulent fluctuation, the boundary flux contribution is zero. Therefore, Eq. (6) can be reduced to

$$K(x_f)=\frac{I_f(t_0+NT)-I_f(t_0)}{NT}. \tag{7}$$

In this way, a link between the axial momentum flux and the change in hydrodynamic impulse of the far-field fluid is established. In order to evaluate $\vec{I}_f(t_0+NT)-\vec{I}_f(t_0)$, one could first calculate $\vec{I}_f(t_0+T)-\vec{I}_f(t_0)$ and then apply the periodic feature to extend the result to the time interval $t_0<t<t_0+NT$. The Appendix provides a detailed derivation showing that $\vec{I}_f(t_0+T)-\vec{I}_f(t_0)=\vec{I}_1$, where $\vec{I}_1=I_1\vec{e}_x$ is the hydrodynamic impulse of all newly discharged vorticity during the jetting period and immediately before the next cycle begins. Extending this relationship to $t_0<t<t_0+NT$, Eq. (7) can be simplified to

$$K\approx fI_1. \tag{8}$$

It is now assumed that the above estimate for the far-field momentum flux is equivalent to the hydrodynamic impulse (times f) of the vortical structure that is ejected from the synthetic jet and then arrives at the far field. This relies on the assumption that once the vortical structure (or simply, the vortex) is completely formed, the effect of the actuator wall can be ignored relative to the effects induced by other vortices. The rationale behind this assumption is that the interaction between the wall and the vortex is strongest during vortex formation but diminishes significantly as the vortex develops and is advected farther away. Practically speaking, the effect of the wall is evidenced by a variation in the radius of the vortex, which several previous studies have observed to quickly reach a nominal value in the near field.[34–36,45]

B. Estimation of hydrodynamic impulse

Having related the time-averaged momentum flux in the far field to the hydrodynamic impulse of the fluid entering the far field, that is, $\vec{I}_1$, we are ready to develop a model to express $\vec{I}_1$ in

terms of the jet-formation parameters. Several studies investigating a starting vortex jet as well as a synthetic jet have employed the classic slug flow model for this purpose, and we briefly introduce this concept. In the slug model, each ejection of fluid is treated as a slug with a constant diameter d and a total length L. The uniform, but time-dependent velocity of the slug is given a sinusoidal form, namely $u_s(t) = \pi f L \sin(2\pi f t)$ with a 50% duty cycle. This velocity program is intended to account for the sinusoidal deflection of the piezo-electric membrane. The momentum flux computed from this slug model is readily obtained as[13]

$$K_s = \frac{\pi^3}{16} f^2 d^2 L^2. \tag{9}$$

While Eq. (9) may predict the functional dependency of K on f, d, and L, the magnitude is often over-predicted (e.g., see Fig. 10(b)) in cases with large stroke ratios at high frequencies.[13] Smith and Glezer[19] and Shuster and Smith[34] regarded the adverse pressure gradient near the jet orifice as being the cause of this discrepancy, whereby some of the ejected momentum is prevented from escaping the near field. In the context of this study, the pressure gradient is tantamount to the actuator suction and the induced effects of existing vortices. Although the direct modeling of these latter near-field processes is also difficult, their resultant effect is contained within the final circulation and configuration of the vortical structure that is generated and leaves the near field. Therefore, we next set out to include these effects to improve the model for $\vec{I}_1$ by analogy with a starting jet and utilizing the extensive amount of previous research on the vortex formation of starting and synthetic jets.

A starting vortex ejected from a round exit generally consists of a large leading vortex (vortex ring with diameter slightly larger than that of the jet orifice) and a slim tail (trailing jet containing smaller-scale vortices). Moreover, Gharib *et al.*[37] have shown that at a certain stroke ratio the circulation of the final leading vortex saturates (an event termed pinch-off), meaning that further increases of the stroke ratio only increase the circulation of the trailing jet. This phenomenon has been well-established for starting jets[37–39,46] and recently confirmed for synthetic or pulsed jets.[34,40,41] To characterize this phenomenon, a non-dimensional parameter called the formation number, L^*/d, was introduced and it is found to be approximately a constant for a jet with the same velocity program and nozzle style. In this study, we first focus on the case with $L/d > L^*/d$, where there is both a leading vortex and a trailing jet and reserve discussion of the $L/d < L^*/d$ case to follow.

We begin again with the uniform, temporally sinusoidal slug flow velocity, $u_s(t)$, which is a 1D jet model, and regard the synthetic jet as being a single-pulsed jet. We note that Krieg and Mohseni[43] have developed a 2D model for starting jets that accounts for the significant effects of various nozzle geometries on, for example, circulation production. These effects are manifested in jets that have non-uniform and/or radial velocity gradients. For orifice nozzle types, Krieg and Mohseni[43] observed non-negligible radial velocity gradients when the diameter-to-depth ratio is large. However, for the orifice nozzle used in this study, the diameter-to-depth ratio is around 1, which will result in a negligible radial expansion of the flow at the jet exit. Hence, a 1D model is deemed appropriate for the current study. As such, the rate of circulation production is $d\Gamma_1/dt = u_s(t)^2/2$, which yields a total circulation of $\Gamma_1 = \pi^2 f L^2/8$ ejected during one cycle.

Given the total circulation, Γ_1, the amounts of circulation that are contained within the leading vortex, Γ_h, and the trailing jet, Γ_t, are now determined. Letting $C = \Gamma_h/\Gamma_1$, which is the fraction of total circulation in the leading vortex, we then have $\Gamma_t/\Gamma_1 = 1 - C$, and it is noted that C is a function of the stroke ratio, L/d. The circulation fraction, C, is obtained by finding the time during the actuator cycle, say t^*, at which the ejected slug length is equal to L^* and then evaluating the circulation at this time. The result is

$$C = 2\left[\frac{t^*}{T} - \frac{\sin(4\pi t^*/T)}{4\pi}\right], \tag{10}$$

where

$$\frac{t^*}{T} = \frac{1}{2\pi} \arccos\left(1 - 2\frac{L^*/d}{L/d}\right). \tag{11}$$

Next, we consider the geometric effects of the vorticity distributions of the leading vortex and trailing jet. This is accomplished by equating the hydrodynamic impulses of each vorticity distribution to those of circular line vortices that have the same respective circulation and which have particular radii, denoted R_h and R_t (see Eq. (12)). These radii represent the geometrical effects and are used to define two vortex geometry parameters as $\alpha = 2R_h/d$ and $\beta = 2R_t/d$, which we refer to as the (non-dimensional) ring radius and the trailing jet radius, respectively. It is important to note that, in general, α and β may be functions of L/d. From Eq. (8), the total momentum flux can then be written as

$$K \approx fI_1 = f\pi\left(R_h^2\Gamma_h + R_t^2\Gamma_t\right) = \frac{\pi^3}{32}f^2d^2L^2\left[\alpha^2 C + \beta^2(1-C)\right]. \tag{12}$$

Finally, the slug model momentum flux, K_s, is used to normalize K yielding

$$\frac{K}{K_s} \approx \frac{1}{2}\left[\alpha^2 C + \beta^2(1-C)\right]. \tag{13}$$

Recall that this derivation, and so the above equation, is only valid for $L/d > L^*/d$, where the vortical structure contains a trailing jet (Eq. (11) ceases to be a real number when $L/d < L^*/d$).

According to Gharib *et al.*,[37] when $L/d < L^*/d$, all of the circulation produced are contained in the leading vortex, meaning that $C \equiv 1$ and from Eq. (13), the normalized momentum flux becomes simply

$$\frac{K}{K_s} \approx \frac{1}{2}\alpha^2, \tag{14}$$

which is a constant if α is also a constant. In such a case, the implication is that the dependency of the momentum flux on L/d is exactly that of the slug model. However, it is important to recall that Eqs. (13) and (14) are based on a single-pulsed jet rather than a synthetic jet. In other words, the effect of the suction phase on the vortex formation, and so I_1, has not yet been explicitly taken into account. These effects are increasingly important for smaller stroke ratios ($<L^*/d$) because when the suction cycle begins, the previously ejected vortex is still in a dynamic formation process and is also in the proximity of the orifice. As a result, the vortex formed during ejection is either ingested back through the orifice or prevented from convecting away from the orifice.[34] Actually, Shuster and Smith[34] have pointed out that the formation vortex ring of a synthetic jet contracts in the near field when L/d is small. This indicates that the geometric configuration of the vortical structure will be altered for a synthetic jet when L/d is small. Hence, α in Eq. (14) will vary with L/d and is also likely to be less than that in Eq. (13) ($L/d > L^*/d$). Moreover, the amount of circulation that is put into the vortex will also be affected (i.e., decreased) as some vorticity will be ingested back through the orifice during suction.[47] Nonetheless, we can retain the total circulation estimate used above and implicitly model the suction effect by absorbing it into the vortex geometry parameters α and β. This will be discussed in more detail in Section V B, where the choices for α and β are analyzed and determined by comparing the model with the measured data.

III. EXPERIMENTAL METHODS

A. Setup and equipment

The experimental setup consists of a hot-wire anemometry system to measure the time-averaged velocity field and is shown in Fig. 3(a). The hot-wire probe is a single platinum-plated probe (Dantec Dynamics 55P16), with a length of 1.25 mm and a diameter of 5 μm. This probe, when operating in the optimal mode through a constant temperature anemometer (Dantec MiniCTA type 54T30), has a frequency response up to 400 kHz. The hot wire is calibrated with fourth order polynomial curve following an iterative procedure,[48] which results in an uncertainty of 2% for air speed greater than 1 m/s and about 20% for air speed less than 0.2 m/s. The hot-wire probe is positioned in the flow field using a two-dimensional traverse system consisting of linear actuators (Zaber TLA60) and translation stages (Zaber TSB). The data acquisition system and the controllers are automated and synchronized using LabVIEW.

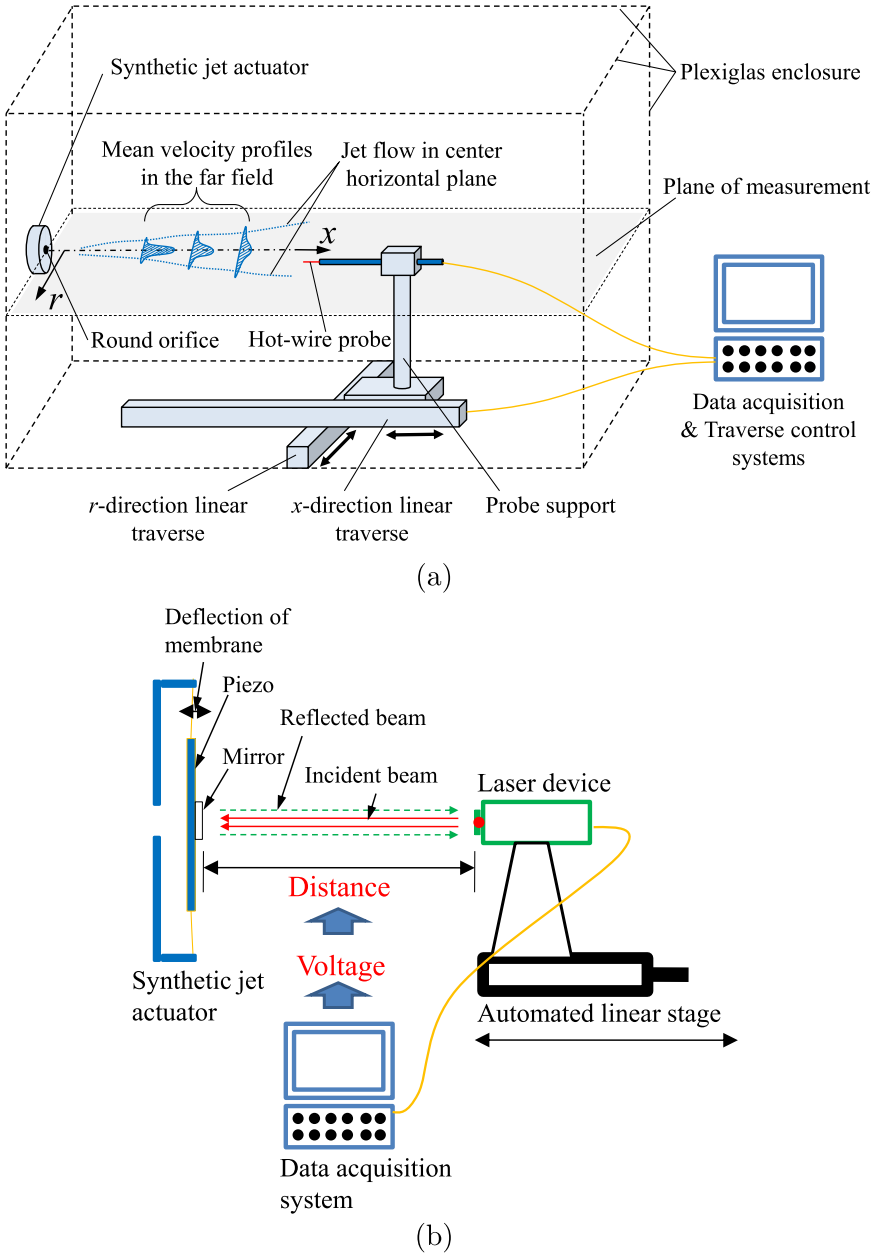

FIG. 3. (a) Schematic of the synthetic jet actuator and hot-wire measurement system. (b) Laser setup for piezo-membrane deflection calibration.

Three different piezoelectric actuators were designed to create different synthetic jet flows. The actuators were all fabricated with the same cavity dimensions, that is, a diameter of 27.8 mm and a depth of 2.0 mm, but different orifice dimensions. The diameters of actuator 1, 2, and 3 are 1.0 mm, 1.5 mm, and 2.0 mm, respectively. The piezoelectric membranes of the actuators are driven by sinusoidal input voltages for which the frequencies and amplitudes can be controlled. These parameters are varied to create synthetic jets with different stroke lengths, L. The test matrix containing the relevant parameters for the synthetic jets is shown in Fig. 4.

The stroke length L is estimated by measuring the deflection of the piezoelectric membrane. This involves a laser measurement,[49] a schematic of which is shown in Fig. 3(b). This experiment uses a laser nano-sensor (LMI LNS type 4) that is capable of detecting the location of a highly reflective surface perpendicular to the laser beam path. For each synthetic jet case, the laser test

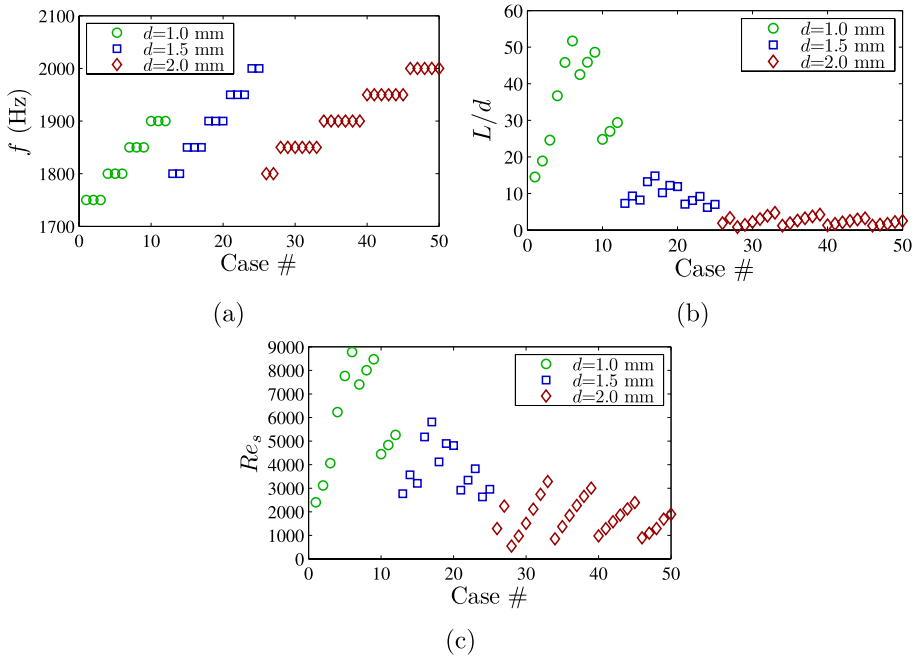

FIG. 4. Test parameters for 50 synthetic jet cases, including (a) driving frequency, f, (b) stroke ratio, L/d, and (c) Reynolds number, Re_s, as estimated from $Re_s = \sqrt{2} f Ld/\nu$ (proposed by Krishnan and Mohseni[49]) at the jet exit. The diameters of the three different actuators are marked by the different symbols in the figure.

is repeated 5 times to give the average p-p deflection of the membrane center. The average standard deviation of the deflection is within 5%. However, combining the error associated with the alignment of the laser setup, the uncertainty in the measurement of L/d is estimated to be around 10%.

B. Experimental calculation of momentum flux

Once the measurements of the velocity field have been acquired, these data are used in Eq. (1) to compute the momentum flux of the synthetic jets; this calculation is performed at each of the axial locations at which measurements were taken. According to Eq. (1), this requires integrating the (square of the) axial velocity in the radial direction from $r = 0$ to ∞. In reality, the jet velocity becomes negligible (i.e., below the resolution of the anemometer) at very large radial locations and so the integration domain can be made finite. However, there still remains the issue of obtaining accurate measurements of the small, but significant velocities at radial distances close to the jet boundary. Namely, the accuracy of the hot-wire anemometer drops when the velocity falls below a certain threshold (the uncertainty is approximately 2% for measured velocity $U > 1$ m/s and 20% for $U < 0.2$ m/s). Fig. 5 shows the error analysis of a typical velocity profile of the far field (SJ33). The measurement of the same velocity profile was repeated six times and the standard deviation of the velocity at each radial location is σ_{std}. The total uncertainty of the velocity, σ, can be estimated using $\sigma = \sqrt{\sigma_{std}^2 + \sigma_m^2}$, where σ_m is the uncertainty associated with the hot-wire anemometry. Fig. 5 verifies that the measurements at large radial distances in the far field are susceptible to more significant errors. Therefore, numerical integration of the velocity data will introduce their associated errors into the calculation of the momentum flux, K. A similar issue was reported by Smith and Swift.[20]

To overcome the above-mentioned challenges, we calculate the momentum flux based on curve fitting a velocity profile using only measurements that exhibit a high signal-to-noise ratio (similar techniques are described in Refs. 19 and 20). For this purpose, we use the classical self-similar turbulent jet velocity profile, which is given by Eq. (15) in Sec. IV. Another advantage of this

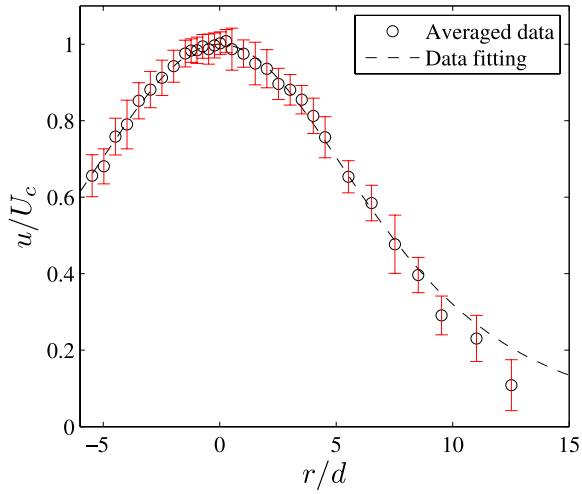

FIG. 5. Velocity profile measurement and error bars at axial location $x/d = 60$ for a sample case (SJ33). The plot shows the averaged data of six different tests of the same velocity profile. Each location of the profile was sampled for 5 s at a rate of 25 kHz during each test. Therefore, the error in this case is a combination of the standard deviation of the measured velocity and the uncertainty associated with the hot-wire anemometry.

approach is that the radial extent of the flow measurement can be further reduced significantly. Fig. 6(a) shows the measured velocity profiles at several axial locations of the same synthetic jet case (SJ33). The data points at large radial distances and with notable deviations are excluded. The curve fitting process is performed in a least squares sense based on the limited data points to determine the jet half-width parameter. The resulting curves are also given in the same plot.

IV. VALIDATION OF THE TURBULENT JET VELOCITY PROFILES

In Sec. III, the reason for fitting an analytical profile to the measured velocities was discussed, along with the experimental method for doing so. However, the accuracy of this method

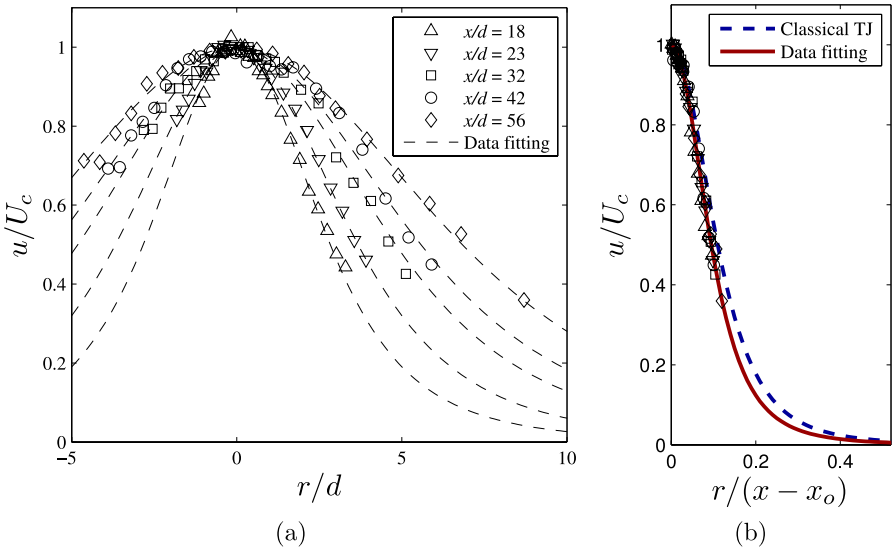

FIG. 6. Velocity profiles at selected axial locations for a sample case (SJ33). (a) Axial velocity normalized by centerline velocity vs. radial location normalized by the orifice diameter; the measured data are fitted to the velocity profile expressed by Eq. (15). (b) Normalized axial velocity vs. radial location normalized by the adjusted axial location based on the jet's virtual origin,[49] x_o, and comparison of the velocity profiles with the classical turbulent jet (TJ) model.

strongly depends on the appropriateness of the analytical velocity profile employed. We use the classical self-similar turbulent jet velocity profile solved by Schlichting[50] (also used by Krishnan and Mohseni[49] to model the far field of a synthetic jet), which is given by

$$u(r,x) = \frac{U_m(x)}{(1 + (r/b_{1/2})^2)^2}, \tag{15}$$

where U_m is the centerline velocity at x and $b_{1/2}$ is the half-width of the jet. Next, we investigate several properties of the measured jet velocity data to validate the use of Eq. (15) for the synthetic jets studied here.

First, the self-similar behavior of the velocity profiles is examined at the far field. Fig. 6(b) plots the velocity measurements from the typical sample case of Fig. 6(a), but with the radial position normalized by the axial location. This figure shows that the jet possesses the assumed self-similarity property as all velocity profiles collapse to one. Note here that the axial location in Fig. 6(b) should be evaluated relative to the virtual origin, x_o (see Krishnan and Mohseni[49] for details). This is an imaginary point along the x-axis as if the far field of the jet linearly spreads out from this point. Therefore, the virtual origin can be obtained by fitting a line to the jet half-width data in the far field and then extending this line to cross with the x-axis, as shown in Fig. 7.

Next, we discuss the turbulent characteristics of the synthetic jets. The flow field for a typical case is shown in Fig. 8; similar results were obtained for other cases. Since the near field is not the focus of this study, the measurement of the flow field is started from an axial distance of $17d$ from the jet orifice, which approximately corresponds to the beginning of the transitional region of a synthetic jet. By comparing the power spectrum plots, it is evident that the energy is transferred from the high- to low-frequency flow structures in both the axial and radial directions. It can be further observed that this energy transfer includes the frequency band corresponding to the turbulent energy. This verifies that turbulence is the dominant mechanism driving the energy transportation in the transitional and far-field regions of the synthetic jets investigated here. Moreover, as the location changes from the transitional region to the far field (starting from $40d$), the turbulent frequency band is shifted away from the driving frequency of the jet. This indicates that the turbulent nature of the far field is less likely to be affected by the jet's pulsation. Therefore, this power spectrum analysis supports the use of a turbulent jet velocity profile to describe the far field of a synthetic jet.

Now, we also note that the derivation of Eq. (15) is based on the assumptions that the streamwise pressure gradient is zero and that K, as computed from Eq. (1), is constant.[49] In other words, the momentum flux calculation based on the curve fitting method is only valid where the conservation

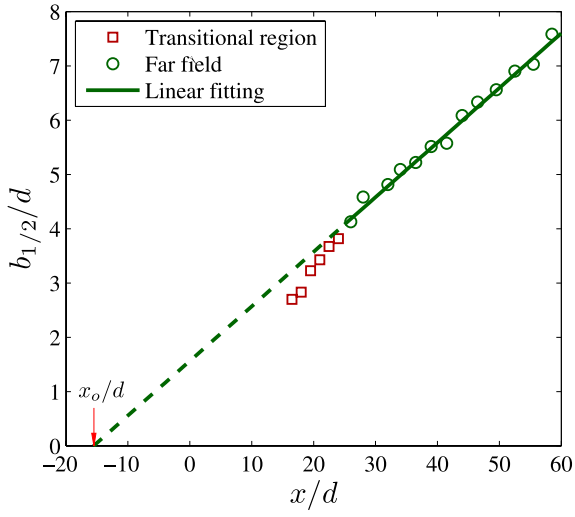

FIG. 7. The variation of jet half-width, $b_{1/2}/d$, in the axial direction for SJ33. A linear variation of $b_{1/2}/d$ vs. x/d can be observed in the far field, and the slope of the fitted line corresponds to the far-field spreading rate of the jet. The intersection between the x-axis and the fitted line gives the virtual origin (x_o) of the far-field jet.

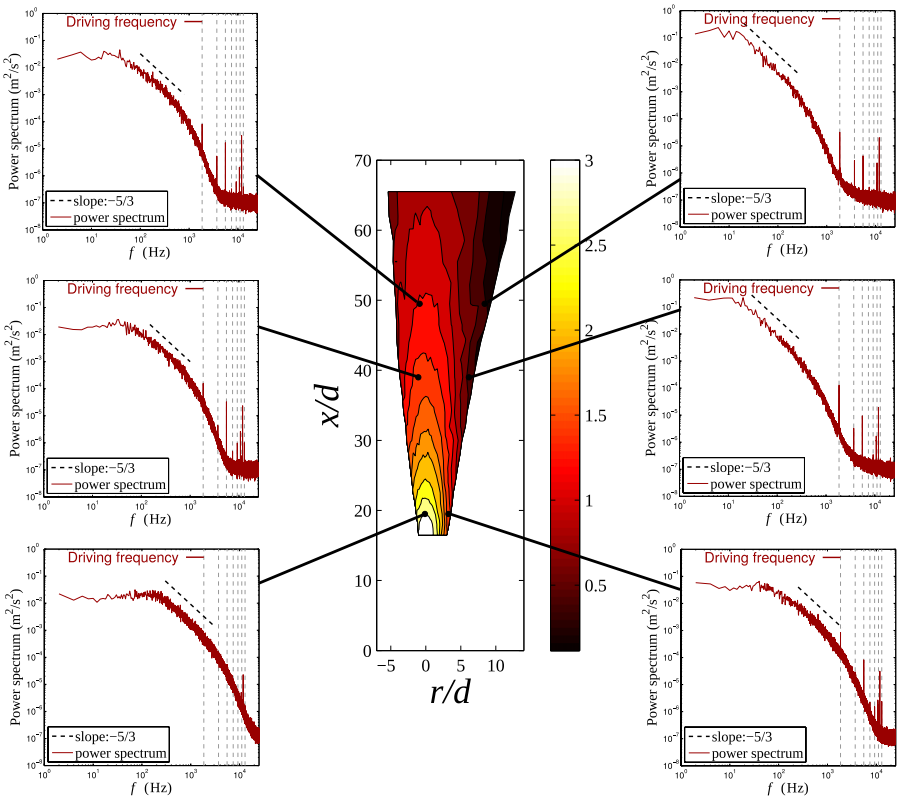

FIG. 8. Power spectrum plots for a sample case (SJ33) for a high-frequency synthetic jet corresponding to (a) locations near the jet centerline and (c) radial locations near the boundary of the jet. The vertical-dashed lines indicate the first seven harmonic frequencies (the 1st harmonic frequency equals the driving frequency of the synthetic jet). (b) Axial velocity contour plot; the unit of the contours is m/s. In order to reduce the number of sampling locations in an axisymmetric jet while capturing the center region of the jet, the flow field measurement was primarily performed on one side of the centerline, with less region covered on the other side. However, the symmetry of the jet flow itself can be indicated from Figs. 5 and 6(a).

of momentum can be confirmed. Here, the axial momentum flux at a given streamwise location, K_x, is computed at different positions in the transitional region and the far field for each synthetic jet. The measured results for selected synthetic jet cases are shown in Fig. 9. In general, it is observed that the momentum fluxes decay toward constant values in the far field, verifying the assumption of constant momentum flux in the far field. Therefore, the asymptotic value of the momentum flux for each synthetic jet is defined as the far-field momentum flux, K. Previous studies[19,20] have also reported similar decreases and leveling off of the momentum flux with increasing streamwise distance. Since the conservation of momentum is a basic physical law, the decay of K_x in the transitional region indicates that other sources of momentum, such as a streamwise pressure gradient, are present. It is also worthwhile to identify the axial location of the region where K_x approaches K, which can be considered as the beginning of the far field in a momentum-conserved sense. For the synthetic jets in this study, this region ranges from about $40d$ to $50d$, which is considerably larger than the commonly accepted value (about $10d$ to $15d$[49,51,52]) obtained by identifying the beginning of the turbulent region of a synthetic jet. Since the near field of a synthetic jet is generally characterized by pulsation while the far field is characterized by turbulence, the result of this study indicates that a transitional region exists where the flow is both pulsatile and turbulent.

V. RESULTS AND DISCUSSIONS

This section compares the experimentally determined far-field momentum flux, K, with the momentum flux computed from the classical slug flow model. Then, the model proposed in

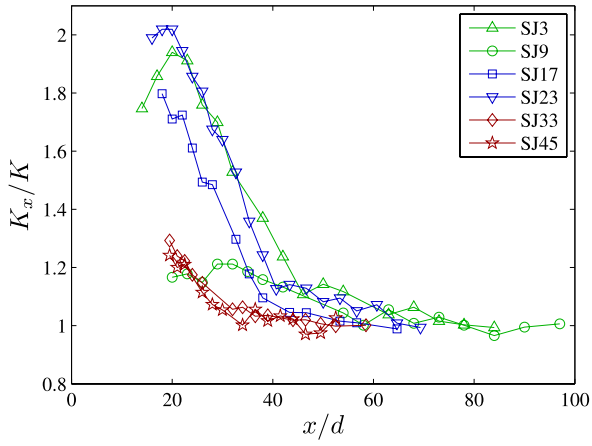

FIG. 9. Streamwise variation of dimensionless momentum flux, K_x/K. Momentum flux, K_x, is normalized by the far-field momentum flux, K. The test case parameters are provided in Fig. 4.

Section II B, which predicts K based on the jet-formation conditions, is discussed. The insight provided by this model offers a new explanation for the momentum drop in the near field of a synthetic jet.

A. Far-field momentum flux

To determine the dependence of the far-field momentum flux on the jet-formation parameters, the dimensional K is first plotted against the stroke ratio, L/d, as shown in Fig. 10(a). As mentioned previously, K is obtained by estimating the asymptotic value of K_x in the far field. It can be seen that for a given actuator, the momentum flux monotonically increases with L/d for the synthetic jets. For a given stroke ratio, a larger diameter actuator results in a larger momentum flux. Both of these trends are intuitive, because each results in more fluid being ejected. To eliminate these actuator-specific dependencies, the momentum flux is normalized by d^4f^2 according to the Buckingham Π theorem, similar to the normalization performed by Krieg and Mohseni.[13] The results are plotted against the stroke ratio in Fig. 10(b), which shows that the actuator dependency has mostly collapsed. The normalized momentum flux computed from the slug model is also plotted for comparison, and according to Eq. (9) predicts a proportionality to $(L/d)^2$. Although the experimental data show an increasing trend, the constant of proportionality that is provided by the slug model is confirmed to result in a significant over-prediction of the measured momentum flux. As mentioned previously, this notable disagreement has also been found in other studies.[20,33,34]

Despite the poor agreement of the measured momentum flux with the slug model observed in Fig. 10(b), the collapse of the actuator dependency along with a clear trend involving the stroke ratio indicates that there is potential for establishing a unified model for the far-field momentum flux of synthetic jets. Moreover, the strong dependence on the stroke ratio, which governs the vortex formation in the near field of a synthetic jet, elucidates the relevance between the far-field momentum flux and the vortex-based analysis proposed in this study. In other words, the theoretical model developed in Section II and represented by Eq. (13) seems to be an apt candidate to rectify the large discrepancy associated with the slug model. Therefore, further analysis and discussion regarding this model will be presented next in Section V B. Before preceding to Sec. V B, we note that this study deals only with high-frequency ($f \sim 10^3$ Hz) synthetic jets, for which the dependency of the normalized momentum flux on the frequency cannot be readily identified in Fig. 10(b). This, again, verifies the finding of Krieg and Mohseni[13] that the dependency of the normalized thrust on the frequency appears to vanish for large-frequency synthetic jets.

B. Momentum flux model for high-frequency synthetic jets

The preliminary analysis described in Section V A has shown that the dimensionless momentum flux, $K/(d^4f^2)$, primarily depends on L/d in the case of high-frequency synthetic jets. In

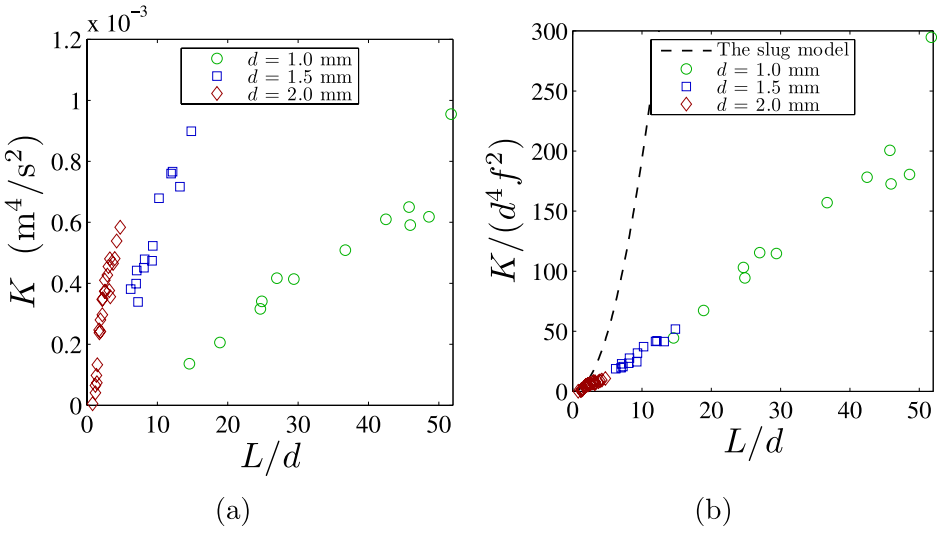

FIG. 10. Measured results for the relationships between far-field momentum flux and stroke ratio for the synthetic jet cases specified in Fig. 4. (a) K vs. L/d and (b) normalized momentum flux, $K/(d^4f^2)$, vs. L/d.

this section, we investigate the dependency of the momentum flux scaled by the slug model, K/K_s, on L/d in order to obtain appropriate values for the parameters (L^*/d, α, and β) of the model that was developed in Section II. Fig. 11(a) plots the experimental K/K_s against stroke ratio, L/d, and shows that the scaled momentum flux initially increases rapidly from near-zero values, comes to a sharp cusp-like peak, and then displays a more gentle decay toward zero as L/d is increased further (note the scale of the horizontal axis is logarithmic). When the stroke ratio approaches the formation number, the physics of the vortex formation drastically changes. As such, the location of the sharp peak in Fig. 11(a) corresponds to the formation number, which is estimated to be $L^*/d = 1.8$. This is consistent with a recent vortex formation study by Lawson and Dawson,[42] which showed that the non-dimensional formation time of the vortex core of a synthetic jet is slightly less than 2. Therefore, we choose the value of $L^*/d = 1.8$ for the model in the current study.

It is worthwhile to note that the formation number is about 4 for starting vortex jets.[37] In fact, even for starting jets, the formation number is found to vary some what between 3.0 and 4.5[37–39,53,54]

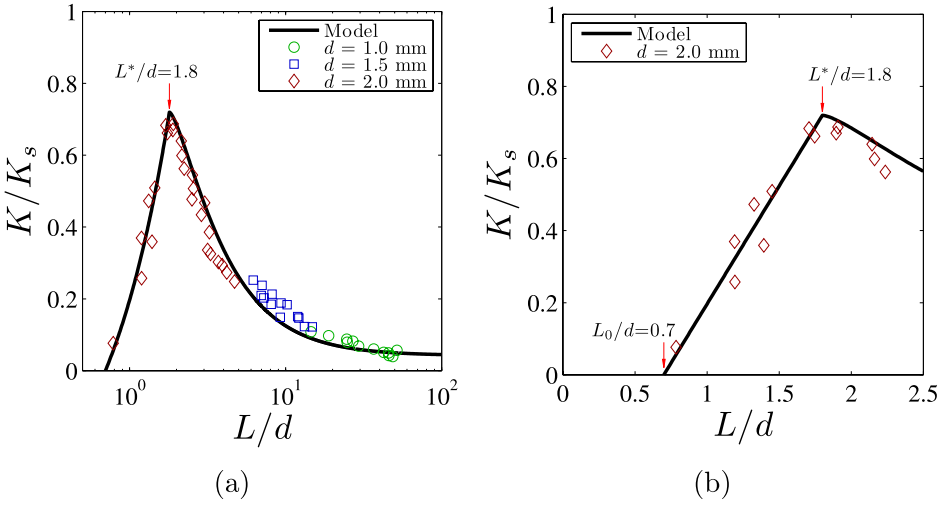

FIG. 11. Relationship between the non-dimensional momentum flux, K/K_s, and the stroke ratio, L/d. K_s is the momentum from the slug model. The model corresponds to $\alpha = 1.2$ and $\beta = 0.29$. (a) Log scale x axis and (b) normal scale x axis focusing on the small L/d region.

for different flow configurations, and the variations can be made quite large by introducing various effects (e.g., temporally variable exit[39,55] and background flow[56]). Although the difference in formation number for synthetic jets should be studied independently in the future, here we hypothesize that it is related to the suction effect as well as the induced effect of the preexisting vortices in the flow.

1. Large stroke ratios: $L/d > L^*/d$

We now discuss in more detail the estimation of the parameters, α and β, for the stroke ratio range corresponding to $L/d > L^*/d$. Also, for convenience, the circulation fractions for the leading vortex and the trailing jet, C and $1 - C$, are plotted in Fig. 12. Recall that α is the non-dimensional radius of the leading vortex ring, which was found to depend primarily on L/d for starting vortex jets according to the studies of Maxworthy[35] and Didden.[36] They further showed that α varies in the range of 1.0–1.4 corresponding to $L/d = 0.5$–3.0, and it tends to saturate around 1.4 when $L/d > 2.0$. Recently, Sullivan *et al.*[45] also showed that α approaches a constant of 1.3 as L/d is increased from 2.0 to 3.0. For synthetic jets, Shuster and Smith[34] have shown that a larger L/d corresponds to a larger value of α and which is approximately 1.2 when $L/d = 3.0$. These studies indicate that the saturated value of α for a synthetic jet seems to be a little lower than that for a starting vortex jet due to the suction effect. Furthermore, we can conclude that α is function of L/d when $L/d < 2.0$, while it can be considered as a constant ranging between 1.2 and 1.4 when $L/d > 2.0$. Since $L^*/d \approx 1.8$ in this study, α is approximately a constant for $L/d > L^*/d$. The value for α can be further corroborated in an empirical way by using the experimental value of $K/K_s \approx 0.7$ near $L/d = L^*/d \approx 1.8$ (where $C = 1$) which yields $\alpha \approx 1.2$. Hence, we opt to use the value $\alpha_0 = 1.2$ in this model, where the subscript is used to denote that it is a constant.

The effect of the trailing jet is reflected by the non-dimensional vortex radius of the trailing jet, β. Here, we determine β empirically by looking at the scaled momentum flux for the larger stroke ratios tested ($30 < L/d < 50$), where the trailing jet momentum flux contribution should dominate over that of the leading vortex (see Fig. 11(b)). The average experimental scaled momentum flux in this range is approximately 0.053 and with a corresponding average of C being about 0.016 along with $\alpha_0 = 1.2$, we estimate $\beta_0 = 0.29$ (again, the subscript implying a constant). The model curve corresponding to these parameters is shown in Fig. 11(a) and is seen to match fairly well with the measured data for the $L^*/d < L/d < 30$ region as well. Next, we discuss the physical meaning

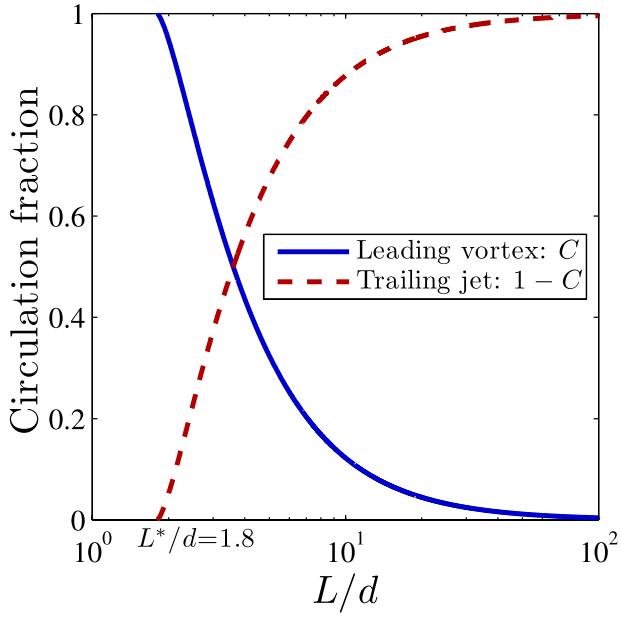

FIG. 12. The fractions of the total circulation that belong to leading vortex, C, and the trailing jet, $1 - C$. These fractions are obtained from the slug model.

of $\beta_0 = 0.29$. On the one hand, several vortex formation studies of starting vortex jets[37,39,43] have shown that the radius of a trailing jet in the near field approximately equals the radius of the jet exit, which corresponds to $\beta = 1$. For synthetic jets, this is also the case according to the study of Lawson and Dawson.[42] However, their study indicates that the trailing jet tends to vanish and its effective vortex radius decreases during its advection to the far field (Figs. 11 and 12 of Lawson and Dawson[42]). This means that β in the far field should be less than 1 for synthetic jets. This is verified in this study as $\beta_0 = 0.29$, which is likely a consequence of the suction effect of the synthetic jet actuator. On the other hand, we note that $\lim_{L/d\to\infty} C = 0$ from Eq. (10) and Fig. 12. As a result, the circulation in the flow, and so the momentum flux, will be dominated by that in the trailing jet and Eq. (13) reduces to $K/K_s \to \beta^2/2$. From Fig. 11(a), it can be observed that the experimental K/K_s tends to approach 0 as $L/d \to \infty$. This intuitively suggests that $\beta \to 0$ in the same limit, which physically means that the effective vortex radius of the trailing jet equals zero or the trailing jet contributes zero impulse to the flow away from the near field. Apparently, this is not the case since $\beta_0 = 0.29$. This result suggests that the trailing jet contributes majorly to the far-field momentum flux of a synthetic jet when L/d is large. This is consistent with the study of Lawson and Dawson,[42] which shows that for large L/d case even when the material flux of impulse (and circulation) into the leading vortex has ceased, the trailing jet can continue to deliver impulse via a vortex force; they describe this as the trailing jet giving the leading vortex an "extra push."

2. Small stroke ratios: $L/d < L^*/d$

Moving on to the $L/d < L^*/d$ region, where there is only a leading vortex and no trailing jet ($C \equiv 1$ or equivalently $\beta \equiv 0$), recall that Eq. (14) predicts a constant value of K/K_s provided that α is a constant. However, this trend is clearly not observed in Fig. 11(a) in which the experimental K/K_s are observed to increase with L/d up to L^*/d. This is related to the fact that the suction phase more significantly affects the still-forming vortex when $L/d < L^*/d$. Similarly, the interaction with the actuator wall will also play a role. From a more physical point of view, for smaller L/d, the vortex will possess lower initial momentum and so will linger in the near field for a longer time and thus be susceptible to these effects. As a result, the final radius of the vortex will be smaller for lower L/d values. This is supported by the literature,[34–36,45] which has shown that the radius of the final vortex increases significantly with L/d when L/d is small.

As mentioned at the end of Section II B, the suction and wall interaction effects are to be accounted for by absorbing them into α. Accordingly, the model will require α to be a function of L/d for values below L^*/d. From Fig. 11(a), it can be inferred that K/K_s should take values from 0 to $\alpha_0^2/2$ as L/d is varied from 0 to L^*/d. To obtain a functionality of α, we further observe the $L/d < L^*/d$ region in Fig. 11(b), and note that the experimental K/K_s data appear to fall on a straight line. This suggests a functionality of $K/K_s = \alpha^2/2 = k[(L/d)/(L^*/d)]$, where the constant of proportionality, k, is obtained from the continuity of K/K_s at L^*/d, namely, $k = \alpha_0^2/2$. Finally, we note that synthetic jets have a critical stroke ratio, L_0/d, below which jetting does not occur.[57] Therefore, L/d can be substituted with $L/d - L_0/d$ to ensure $K/K_s = 0$ at $L/d = L_0/d$. This gives $\alpha = \alpha_0\sqrt{(L - L_0)/(L^* - L_0)}$ for $L/d < L^*/d$, which predicts that for synthetic jets α could be lower than 1 when L/d is small. Actually, this is supported by the study of Shuster and Smith,[34] which shows that α is between 0.7 and 0.75 for a synthetic jet with $L/d = 1$. Based on the above analysis, the modified model for the momentum flux can be written as

$$\frac{K}{K_s} = \begin{cases} \dfrac{1}{2}\alpha_0^2\left(\dfrac{L - L_0}{L^* - L_0}\right) & L/d < L^*/d \\ \dfrac{1}{2}\left[\alpha_0^2 C + \beta_0^2(1 - C)\right] & L/d > L^*/d \end{cases}, \tag{16}$$

where C is obtained from Eqs. (10) and (11). In this study, L_0 is determined to be 0.7 by fitting this model to data in the $L/d < L^*/d$ region. This value is comparable with those obtained by Holman *et al.*[57] ($L_0/d \approx 0.5$) and Shuster and Smith[34] ($L_0/d \approx 0.6$).

Before concluding this study, the necessity that α be a function of L/d when $L/d < L^*/d$ can be further corroborated by appealing to the Norbury vortex family[58] with α_N varying between 0 and

$\sqrt{2}$ (α_N is the non-dimensional mean core radius). The use of Norbury vortices has been shown to yield good accuracy in a vortex formation study of a starting jet by Mohseni and Gharib.[38] In the Norbury vortex family, the vortex corresponding to $\alpha_N = 0$ is a circular line vortex (thin core vortex), the vorticity of which is concentrated on an infinitesimal core; while the vortex corresponding to $\alpha_N = \sqrt{2}$ is actually the axis-touching Hill's vortex that has a finite core area and distributed vorticity. From Fig. 6 of Norbury,[58] the ratio between impulse and circulation, I/Γ, for the thin core vortex and the Hill's vortex can be calculated to be πR^2 and $5.02R^2$ (R is the vortex radius), respectively. This means that if a thin core vortex has the same amount of circulation and impulse as a Hill's vortex, the radius of the thin core vortex must be larger than that of the Hill's vortex. Now consider a starting vortex jet, the formed vortex in the near field may closely resemble a thin core vortex ring when the stroke ratio is small ($L/d < L^*/d$); however, as L/d increases, the core of the formed vortex will thicken, much like the core of a Norbury vortex does (by definition) with increasing α_N. Recall that the thin core vortex model is applied in this study regardless of the actual thickness of the core and, as a result, it requires a larger radius of the thin core vortex to hold the same amount of circulation and impulse of an actual vortex with finite core radius. This means that α has to increase in response to a thickened vortex core when L/d is increased. For synthetic jets with small L/d, the strong suction effect in the near field could cause α to be smaller than that of starting jets;[34] nevertheless, the above discussion about the correlation between α and L/d should still be valid.

To summarize, the measured data are found to agree with the values obtained with the model when $L/d > L^*$. In the $L/d < L^*/d$ region, although the overall trend in the data is in agreement with the model, the estimation of α depends on empirical fitting. Therefore, any future work should focus on the vortex formation process of synthetic jets to provide a more rigorous and accurate model for α.

Next, we emphasize the significance of this study. The primary contribution of this model is that it addresses the difficulty of predicting the far-field momentum flux of a synthetic jet caused by complex near-field effects. By estimating the impulse of the vortices exiting the near field, it avoids dealing directly with the effects of the time-dependent near field. The secondary contribution of this model is that it predicts a decrease of the normalized far-field momentum flux with increasing L/d for synthetic jets with $L/d > L^*/d$. This trend is due to an increasing circulation fraction of the formed trailing jet while its contribution to the impulse per unit circulation is much less than that of the leading vortex. With the non-dimensional vortex radius of the trailing jet (β) found to be approximately 0.29, it indicates that a major part of the trailing vortices might be decelerated or ingested during the suction phase. Nevertheless, $\beta > 0$ still confirms that the contribution of the trailing jet vortices to the overall far-field momentum flux of a synthetic jet is not negligible, especially when L/d is large. Therefore, this fundamentally explains how the pressure gradient caused by suction decreases the momentum flux of a synthetic jet in the near field.

There are multiple applications where this model can be utilized. For example, to predict the far-field features (spreading rate and decay rate) of synthetic jets in quiescent flow, the far-field momentum flux is required according to our recent study.[22] The model presented here provides far-field momentum flux based on the actuation parameters of a synthetic jet. Therefore, this model could also be useful in the application of high-frequency vortex thruster since thrust is closely related to the far-field momentum flux. Flow control is another field where this model might be applied. Such applications usually involves the interaction between a synthetic jet and a background crossflow.[6,16,26,30] One concern here might be that the roll-up of the vortex sheet is affected by the crossflow near the jet exit, causing the vortex ring becomes non-axisymmetric.[6] If this is the case, the model developed in this work might not accurately capture the impulse carried by the vortex ring. However, we argue that for larger-blowing-ratio cases where the synthetic jet velocity dominates the background flow, this model could still be valid. This is because the influence of the crossflow is relatively small compared with the strong vortex ring formed by the synthetic jet actuator. Further limitations of this model are provided below. It is apparent that this model is developed for high-frequency axisymmetric synthetic jets. For low-frequency cases, the vortex geometry parameters, α and β, as well as the pinch-off process could be different from those for high-frequency cases. This is primarily due to the near-field background flow being less influenced

by the preceding vortices and the suction flow if the actuation frequency is low. The extension of this model to non-axisymmetric jets should also be handled with caution. Take the rectangular synthetic jet, for example, a similar approach might be applied to predict the far-field momentum flux by estimating the impulse of the fully developed vortical structure that is created during each jetting cycle. However, this is rather difficult due to 3D effects. Namely, an "axis switching" phenomenon[59,60] causes a dramatic change in the shape of an elliptical vortex ring during its early transition in the near field. As a result, this morphing behavior of the vortex ring makes it difficult to estimate the ring shape and the circulation distribution around the final vortex ring, as well as the parameters associated with the pinch-off process.

VI. CONCLUSIONS

The purpose of this study was to develop a model that predicts the far-field momentum flux of high-frequency axisymmetric synthetic jets. To find the relationship between the far-field momentum flux and the actuation parameters, the former is addressed by calculating the hydrodynamic impulse of vortical structures in the flow. With the flow assumed to be fully developed and periodic, the total induced effect of external vortical structures on a fully formed vortex is shown to vanish during the evolution of the vortex into the far field. Therefore, the momentum flux of the far field can be converted to the hydrodynamic impulse of a completely formed vortex, which can be further modeled using jet-formation conditions, such as the stroke length, L, the orifice diameter, d, and the frequency, f.

The measured momentum flux is first studied by analyzing the relationship between the far-field momentum flux, K, and the stroke ratio, L/d. The results show a strong dependence of K on L/d. Moreover, the model proposed in this study predicts that the scaled momentum flux, K/K_s, decreases when L/d is increased for the $L/d > L^*/d$ cases. It is also found that K/K_s increases with L/d for the $L/d < L^*/d$ cases. The matching between the experiment and model is reasonable for both large and small stroke ratios. In addition, the experimental results also indicate that the scaled momentum flux K/K_s exhibits very little dependency on the frequency for high-frequency synthetic jets. Finally, but most importantly, the geometry parameter, β, which corresponds to the effective radius of the trailing jet, is found to be 0.29. This indicates that the trailing vortices does contribute to the final momentum flux in the far field, and this contribution becomes dominant when L/d is large. However, with β being much smaller than 1, it suggests that the effect of the suction phase decelerates or ingests the trailing vortices so that the impulse of the trailing jet is significantly lowered after exiting the near field. This provides an auxiliary explanation for the momentum flux decay in the near field, as observed by other researchers.

In conclusion, this momentum flux model creates a link between the normalized far-field momentum flux of a synthetic jet and the stroke ratio of the actuator. For the first time, this model enables the prediction of the far-field momentum flux for synthetic jets, based on the jet-formation conditions. This model also contributes to a turbulent jet model that predicts the far-field features of synthetic jets using only the jet-formation conditions (L, d, and f) without any measurements of the flow field.

ACKNOWLEDGMENTS

This work is supported by a grant from the Office of Naval Research. We would like to appreciate the valuable comments provided by Dr. A. DeVoria on estimating the circulation fractions of the leading vortex and the trailing jet. We would also like to thank Dr. M. Kreig for sharing helpful discussions and comments.

APPENDIX: CHANGE IN HYDRODYNAMIC IMPULSE

This section describes the derivation that connects the change in the hydrodynamic impulse of the far field ($\vec{I}_f(t_0 + T) - \vec{I}_f(t_0)$) to the hydrodynamic impulse of a newly generated vortex of the

jet ($\vec{I}_1$). Since the flow vanishes at infinity, a finite volume V_f bounded by $S_1 + S_2 + S_3$ is defined to contain the far-field flow of the jet, as shown in Fig. 2. On the other hand, N' volume sections from V_1 to $V_{N'}$ are defined to contain the N' individual vortical structures before the far field. Now, at time $t = t_0$, we consider all the fluid inside the volume, $V_f + V_{N'}$, as being a joined controlled mass, denoted by m_f; this controlled mass would be occupying V_f at time $t = t_0 + T$ when $\Gamma_{N'}$ (corresponding to the hatched region in Fig. 2) has completely entered the far field. Next, the hydrodynamic impulses of the controlled mass at time t_0 and $t_0 + T$ are evaluated separately as

$$\vec{I}_{m_f(t_0)} = \vec{I}_f(t_0) + \vec{I}_{N'}(t_0) = \frac{1}{2}\int_{V_f(t_0)+V_{N'}(t_0)} \vec{x} \times \vec{\omega} \mathrm{d}V \tag{A1a}$$

and

$$\vec{I}_{m_f(t_0+T)} = \vec{I}_f(t_0 + T) = \frac{1}{2}\int_{V_f(t_0+T)} \vec{x} \times \vec{\omega} \mathrm{d}V, \tag{A1b}$$

where $\vec{I}_{N'}$ represents the hydrodynamic impulse of the fluid inside volume $V_{N'}$. The definition of the hydrodynamic impulse in the above equation indicates that vorticity is the only source contributing to the hydrodynamic impulse. This means that, instead of having to calculate the entire flow field, momentum estimation might be possible by focusing only on the vortical structures.

To further estimate $\vec{I}_f(t_0 + T) - \vec{I}_f(t_0)$, the property of the isolated vortices (see Saffman,[44] page 58) is applied to the controlled mass, m_f, so the corresponding rate of change of hydrodynamic impulse is written as

$$\frac{d\vec{I}_{m_f}}{dt} = \int_{m_f} \vec{F} \mathrm{d}x + \int_{m_f} \vec{u}_e \times \vec{\omega} \mathrm{d}V, \tag{A2}$$

where $\vec{F}$ is the non-conservative external body force, which is zero everywhere for a free jet; $\vec{u}_e$ accounts for both the velocity of m_f relative to the background flow and the velocity induced by external vortices. Therefore, combining Eqs. (A1a), (A1b), and (A2) yields

$$\vec{I}_f(t_0 + T) - \vec{I}_f(t_0) = \vec{I}_{N'}(t_0) + \int_{t_0}^{t_0+T}\int_{m_f} \vec{u}_e \times \vec{\omega} \mathrm{d}V \mathrm{d}t. \tag{A3}$$

Further note that no background flow is considered in this study, so only the vortical structures outside the far field contribute to $\vec{u}_e$, i.e., the $N' - 1$ vortices from Γ_1 to $\Gamma_{N'-1}$. For simplification purposes, a new quantity, $\Delta I_{i,j}(t_0)$, is defined here as

$$\Delta I_{i,j}(t_0) = \int_{t_0}^{t_0+T}\int_{i\to j} \vec{u}_e \times \vec{\omega} \mathrm{d}V \mathrm{d}t, \tag{A4}$$

where i and j are the subscripts of the vortical structures, Γ_i and Γ_j, respectively; $i \to j$ denotes the induced effect of Γ_i on Γ_j. Therefore, $\Delta I_{i,j}(t_0)$ represents the change in the hydrodynamic impulse of Γ_j due to the induced effect of Γ_i from $t = t_0$ to $t = t_0 + T$. Consequently, Eq. (A3) becomes

$$\vec{I}_f(t_0 + T) - \vec{I}_f(t_0) = \vec{I}_{N'}(t_0) + \sum_{i=1}^{N'-1} (\Delta I_{i,N'}(t_0) + \Delta I_{i,f}(t_0)). \tag{A5}$$

Note that, here, Γ_f represents all of the vortical structures in the far field, as shown in Fig. 2. This equation indicates that the change in the hydrodynamic impulse in the far field equals the impulse carried by the fluid entering the far field plus any effect induced by the other vortical structures in the jet.

At this stage, an estimation of the momentum flux in the far field is made using Eqs. (7) and (A5). However, there is still a gap between the impulse of the vortical structures and the forming conditions of the jet (L, d, f). The quantities in Eq. (A5) need to be further calculated by considering the vortex formation process in the near field. Here, the fluid contained inside $V_{N'}$ at $t = t_0$ (the hatched region in Fig. 2) is treated as a control mass. The vortical structure corresponding to $V_{N'}$ is $\Gamma_{N'}$, the history of which can be traced back to Γ_1 at $t = t_0 - (N' - 1)T$, immediately after

the vortical structure was formed. Therefore, by setting $t_0 = N'T$, this control mass corresponds to Γ_j and V_j at $t = jT$ under the periodic assumption. According to Eq. (A2), the change in the hydrodynamic impulse of this control mass from $t = jT$ to $t = (j+1)T$ can be expressed as

$$\vec{I}_j((j+1)T) - \vec{I}_j(jT) = \sum_{i=1, i\neq j}^{N'} \Delta I_{i,j}(jT) + \Delta I_{f,j}(jT), \quad \text{for } j = 1, \ldots, N'-1. \tag{A6}$$

As a result, $\vec{I}_{N'}(t_0)$ in Eq. (A5) is related to $\vec{I}_1(T)$ by

$$\begin{aligned}\vec{I}_{N'}(t_0) - \vec{I}_1(T) &= \vec{I}_{N'}(N'T) - \vec{I}_1(T)\\ &= \sum_{j=1}^{N'-1} (\vec{I}_j((j+1)T) - \vec{I}_j(jT))\\ &= \sum_{j=1}^{N'-1} \left(\sum_{i=1, i\neq j}^{N'} \Delta I_{i,j}(jT) + \Delta I_{f,j}(jT) \right).\end{aligned} \tag{A7}$$

Here, $\Delta I_{i,j}(kT)$ stays the same for any integer k due to periodicity of the flow. Therefore, $\Delta I_{i,j}(jT)$ and $\Delta I_{f,j}(jT)$ can be reduced in the above equation to $\Delta I_{i,j}$ and $\Delta I_{f,j}$, respectively, for any integer j. Also note that $\Delta I_{i,j} = -\Delta I_{j,i}$ because the induced effect of Γ_i on Γ_j is exactly the opposite of the effect of Γ_j on Γ_i, so Eq. (A7) can be further simplified to

$$\begin{aligned}\vec{I}_{N'}(t_0) - \vec{I}_1(T) &= \cancelto{0}{\sum_{j=1}^{N'-1} \sum_{i=1, i\neq j}^{N'-1} \Delta I_{i,j}} + \sum_{j=1}^{N'-1} (\Delta I_{N',j} + \Delta I_{f,j})\\ &= \sum_{j=1}^{N'-1} (\Delta I_{N',j} + \Delta I_{f,j}).\end{aligned} \tag{A8}$$

Now, combining Eqs. (A5) and (A8) yields

$$\begin{aligned}\vec{I}_f(t_0 + T) - \vec{I}_f(t_0) &= \vec{I}_1(T) + \sum_{j=1}^{N'-1} (\Delta I_{N',j} + \Delta I_{f,j}) + \sum_{i=1}^{N'-1} (\Delta I_{i,N'} + \Delta I_{i,f})\\ &= \vec{I}_1(T).\end{aligned} \tag{A9}$$

Eq. (A9) demonstrates that the change in the hydrodynamic impulse of the far field during one period equals the hydrodynamic impulse of the newly generated vortex, which is located outside the near field. Apparently, all of the induced effects between the vortices eventually cancel each other out during their evolution to the far field.

[1] L. Cattafesta and M. Sheplak, "Actuators for active flow control," Annu. Rev. Fluid Mech. **43**, 247–272 (2011).
[2] K. Mohseni and R. Mittal, *Synthetic Jets: Fundamentals and Applications* (CRC Press, 2014).
[3] M. Amitay and A. Glezer, "Role of actuation frequency in controlled flow reattachment over a stalled airfoil," AIAA J. **40**, 209–216 (2002).
[4] M. Amitay and A. Glezer, "Controlled transients of flow reattachment over stalled airfoils," Int. J. Heat Fluid Flow **23**, 690–699 (2002).
[5] S. Zhang and S. Zhong, "Experimental investigation of flow separation control using an array of synthetic jets," AIAA J. **48**, 611–623 (2010).
[6] M. Jabbal and S. Zhong, "Particle image velocimetry measurements of the interaction of synthetic jets with a zero-pressure gradient laminar boundary layer," Phys. Fluids **22**, 063603 (2010).
[7] M. Amitay, D. R. Smith, V. Kibens, D. Parekh, and A. Glezer, "Aerodynamic flow control over an unconventional airfoil using synthetic jet actuators," AIAA J. **39**, 361–370 (2001).
[8] R. Mittal and P. Rampunggoon, "On the virtual aeroshaping effect of synthetic jets," Phys. Fluids **14**, 1533–1536 (2002).
[9] J. Gilarranz, L. Traub, and O. Rediniotis, "A new class of synthetic jet actuators—Part II: Application to flow separation control," J. Fluids Eng. **127**, 377–387 (2005).
[10] R. Raju, R. Mittal, and L. Cattafesta, "Dynamics of airfoil separation control using zero-net-mass-flux forcing," AIAA J. **46**, 3103–3115 (2008).
[11] D. Williams, W. Kerstens, J. Pfeiffer, R. King, and T. Colonius, "Unsteady lift suppression with a robust closed loop controller," in *Active Flow Control II* (Springer, Berlin, Heidelberg, 2010), pp. 19–30.

[12] K. Mohseni, "Pulsatile vortex generators for low-speed maneuvering of small underwater vehicles," Ocean Eng. **33**, 2209–2223 (2006).
[13] M. Krieg and K. Mohseni, "Thrust characterization of pulsatile vortex ring generators for locomotion of underwater robots," IEEE J. Oceanic Eng. **33**, 123–132 (2008).
[14] L. Yuan and R. Street, "Trajectory and entrainment of a round jet in crossflow," Phys. Fluids **10**, 2323–2335 (1998).
[15] L. Yuan, R. Street, and J. Ferziger, "Large-eddy simulations of a round jet in crossflow," J. Fluid Mech. **379**, 71–104 (1999).
[16] N. Schaeffler and L. Jenkins, "Isolated synthetic jet in crossflow: Experimental protocols for a validation dataset," AIAA J. **44**, 2846–2856 (2006).
[17] S. Ugrina, "Experimental analysis and analytical modeling of synthetic jet cross flow interaction," Ph.D. thesis, University of Maryland, 2007.
[18] X. Xia and K. Mohseni, "An experimental and modeling investigation of synthetic jets in a coflow wake," Int. J. Flow Control **3**, 19–35 (2011).
[19] B. Smith and A. Glezer, "The formation and evolution of synthetic jets," Phys. Fluids **10**, 2281–2297 (1998).
[20] B. Smith and G. Swift, "Synthetic jets at larger Reynolds number and comparison to continuous jets," AIAA Paper 2001-3030, 2001.
[21] B. Smith and G. Swift, "A comparison between synthetic jets and continuous jets," Exp. Fluids **34**, 467–472 (2003).
[22] X. Xia and K. Mohseni, "Axisymmetric synthetic jets: A momentum-based modeling approach," AIAA Paper 2012-1246, 2012.
[23] D. Paxson, M. Wernet, and W. John, "Experimental investigation of unsteady thrust augmentation using a speaker-driven jet," AIAA J. **45**, 607–614 (2007).
[24] L. A. Ruiz, R. W. Whittlesley, and J. O. Dabiri, "Vortex enhanced propulsion," J. Fluid Mech. **668**, 5–32 (2010).
[25] V. Troshin and A. Seifert, "Performance recovery of a thick turbulent airfoil using a distributed closed-loop flow control system," Exp. Fluids **54**, 1443 (2013).
[26] D. Smith, "Interaction of a synthetic jet with a crossflow boundary layer," AIAA J. **40**, 2277–2288 (2002).
[27] I. Milanovic and K. Zaman, "Synthetic jets in crossflow," AIAA J. **43**, 929–940 (2005).
[28] M. Jabbal and S. Zhong, "The near wall effect of synthetic jets in a boundary layer," Int. J. Heat Fluid Flow **29**, 119–130 (2008).
[29] M. Ramasamy, J. Wilson, and P. Martin, "Interaction of synthetic jet with boundary layer using microscopic particle image velocimetry," J. Aircr. **47**, 404–422 (2010).
[30] O. Sahni, J. Wood, K. Jansen, and M. Amitay, "Three-dimensional interactions between a finite-span synthetic jet and a crossflow," J. Fluid Mech. **671**, 254–287 (2011).
[31] J. Vasile and M. Amitay, "Interactions of an array of finite span synthetic jets and crossflow," AIAA J. **51**, 2503–2512 (2013).
[32] A. Glezer, "The formation of vortex rings," Phys. Fluids **31**, 3532–3542 (1988).
[33] M. Jabbal, J. Wu, and S. Zhong, "The performance of round synthetic jets in quiescent flow," Aeronaut. J. **110**(1108), 385–393 (2006).
[34] J. M. Shuster and D. R. Smith, "Experimental study of the formation and scaling of a round synthetic jet," Phys. Fluids **19**, 45109 (2007).
[35] T. Maxworthy, "Some experimental studies of vortex rings," J. Fluid Mech. **80**, 465–495 (1977).
[36] N. Didden, "On the formation of vortex rings: Rolling-up and production of circulation," Z. Angew. Math. Phys. **30**, 101–116 (1979).
[37] M. Gharib, E. Rambod, and K. Shariff, "A universal time scale for vortex ring formation," J. Fluid Mech. **360**, 121–140 (1998).
[38] K. Mohseni and M. Gharib, "A model for universal time scale of vortex ring formation," Phys. Fluids **10**, 2436–2438 (1998).
[39] K. Mohseni, H. Ran, and T. Colonius, "Numerical experiments on vortex ring formation," J. Fluid Mech. **430**, 267–282 (2001).
[40] I. Choutapalli, A. Krothapalli, and J. Arakeri, "An experimental study of an axisymmetric turbulent pulsed air jet," J. Fluid Mech. **631**, 23–63 (2009).
[41] E. Aydemir, N. Worth, and J. Dawson, "The formation of vortex rings in a strongly forced round jet," Exp. Fluids **52**, 729–742 (2012).
[42] J. Lawson and J. Dawson, "The formation of turbulent vortex rings by synthetic jets," Phys. Fluids **25**, 105113 (2013).
[43] M. Krieg and K. Mohseni, "Modelling circulation, impulse, and kinetic energy of starting jets with non-zero radial velocity," J. Fluid Mech. **719**, 488–526 (2013).
[44] P. Saffman, *Vortex Dynamics* (Cambridge University Press, Cambridge, 1992).
[45] I. Sullivan, J. Niemela, R. Hershberger, D. Bolster, and R. Donnelly, "Dynamics of thin vortex rings," J. Fluid Mech. **609**, 319–347 (2008).
[46] M. Shusser and M. Gharib, "Energy and velocity of a forming vortex ring," Phys. Fluids **12**, 618–621 (2000).
[47] M. Krieg and K. Mohseni, "Pressure and work analysis of unsteady, deformable, axisymmetric, jet producing cavity bodies," J. Fluid Mech. **769**, 337–368 (2015).
[48] A. Johnstone, M. Uddin, and A. Pollard, "Calibration of hot-wire probes using non-uniform mean velocity profiles," Exp. Fluids **39**, 525–532 (2005).
[49] G. Krishnan and K. Mohseni, "Axisymmetric synthetic jets: An experimental and theoretical examination," AIAA J. **47**, 2273–2283 (2009).
[50] H. Schlichting, *Boundary-Layer Theory* (McGraw-Hill Book Company, New York, 1979).
[51] S. Mallinson, G. Hong, and J. Reizes, "Some characteristics of synthetic jets," AIAA Paper 99-3651, 1999.
[52] J. Cater and J. Soria, "The evolution of round zero-net-mass-flux jets," J. Fluid Mech. **472**, 167–200 (2002).
[53] M. Rosenfeld, E. Rambod, and M. Gharib, "Circulation and formation number of laminar vortex rings," J. Fluid Mech. **376**, 297–318 (1998).
[54] J. Dabiri and M. Gharib, "Fluid entrainment by isolated vortex rings," J. Fluid Mech. **511**, 311–331 (2004).

[55] J. Dabiri and M. Gharib, "Starting flow through nozzles with temporally variable exit diameter," J. Fluid Mech. **538**, 111–136 (2005).
[56] P. Krueger, J. Dabiri, and M. Gharib, "The formation number of vortex rings formed in a uniform background co-flow," J. Fluid Mech. **556**, 147–166 (2006).
[57] R. Holman, Y. Utturkar, R. Mittal, B. Smith, and L. Cattafesta, "Formation criterion for synthetic jets," AIAA J. **43**, 2110–2116 (2005).
[58] J. Norbury, "A family of steady vortex rings," J. Fluid Mech. **57**, 417–431 (1973).
[59] M. R. Dhanak and B. Bernardinis, "The evolution of an elliptic vortex ring," J. Fluid Mech. **109**, 189–216 (1981).
[60] T. V. Buren, E. Whalen, and M. Amitay, "Vortex formation of a finite-span synthetic jet: Effect of rectangular orifice geometry," J. Fluid Mech. **745**, 180–207 (2014).